ADVANCED MATERIALS
www.advmat.de

Giga-Voxel Multiscale Composite Architecture Mirrored Through a Data-to-Model Closed-Loop Digital Twin

Siwon Yu, Seungsoo Jang, Young Seok Cho, Seunggyu Park, Jun Yeon Hwang, Soon Hyung Hong,* Thomas James Marrow, and Kang Taek Lee**

Giga-voxel digital models offer abundant geometric detail; however, no mainstream method currently exists to efficiently distribute individual voxels across massive image volumes, and designing complex anisotropic composite materials remains infeasible due to the absence of promising methods. Herein, we propose a systematic digital twin workflow tailored for generating high-fidelity virtual representations of anisotropic composite microstructures and giga-voxel meso-structural models, leveraging a harmonious integration of top-down image-based modeling and bottom-up data-driven generation. Our study demonstrates the efficacy of micro-digital representations as foundational building blocks within a continuum of digital assembly processes tailored for mesostructural models. Utilizing 3D image data, specifically X-ray tomography, our data-driven modeling meticulously characterizes the geometric attributes of the experimentally observed objects, thereby facilitating the creation of digital unit twins, each endowed with distinct identities assigned through a random seed generation. The closed-loop system provides feedback mechanism between data and model to ensure the 3D quality of the generated models. For hierarchical organization at the giga-voxel level, the digital unit twins are methodically expanded into cohesive 3D architectures based on assembly relationship at length scales of more than four orders of magnitude. Remarkably, this hierarchical model provides intricate insight into micro-to-macro geometrics while preserving the intrinsic microstructure.

1. Introduction

In the context of the 4th Industrial Revolution, the transition from top–down to bottom–up manufacturing processes[1–3] necessitates the exploration of novel conceptual modeling capable of describing physical objects comprehensively, spanning from microstructure to macro-architecture.[4–6] In response to the growing need for more adaptable image modeling, the concept of a "digital twin" has gained great attention. Digital twin technology enables the investigation of structures by creating and simulating virtual representations of materials or systems.[7–9] This modeling approach mirrors the appearance, information, and structure of physical objects in the real world,[7] across a variety of time and spatial scales, and environments, and can be continuously updated through dynamic data synchronization between the physical and digital twins.[8] These capabilities have positioned the digital twin as a key technology to interconnect the major intelligence technologies of Metaverse, IoT, AI, and computer vision.[9]

S. Yu, S. Jang, K. T. Lee
Department of Mechanical Engineering
KAIST
Daejeon 34141, Republic of Korea
E-mail: leekt@kaist.ac.kr

S. Yu, T. J. Marrow
Department of Materials
University of Oxford
Oxford OX1 3PH, UK

Y. S. Cho
Trinity Engineering
Seoul 07997, Republic of Korea

The ORCID identification number(s) for the author(s) of this article can be found under https://doi.org/10.1002/adma.202510559

DOI: 10.1002/adma.202510559

S. Park, J. Y. Hwang
Institute of Advanced Composite Materials
Korea Institute of Science and Technology, (KIST)
Jeonbuk 55324, Republic of Korea
E-mail: Junyeon.Hwang@kist.re.kr

S. H. Hong
Department of Material Science and Engineering
KAIST
Daejeon 34141, Republic of Korea
E-mail: shhong@kaist.ac.kr

S. H. Hong
Nanotechnology Research Institute
Jiaxing University
Jiaxing 314001, China

K. T. Lee
KAIST Graduate School of Green Growth and Sustainability
Daejeon 34141, Republic of Korea

K. T. Lee
KAIST InnoCORE PRISM-AI Center
KAIST
Daejeon 34141, Republic of Korea

The digital twin is a closed-loop system that integrates both "top–down" and "bottom–up" approaches. The top-down approach utilizes high-resolution tomographic images obtained through advanced 3D scanning techniques such as focused ion beam-scanning electron microscopy (FIB-SEM) and X-ray computed microtomography (μCT) to construct realistic microstructural voxel image models.[10,11] Significant efforts have been directed toward improving image segmentation and reconstruction processes to accurately identify various geometric features and topologies within the raw data.[12] For example, Ali et al. developed deep convolutional neural networks (DCNN) to accurately segment μCT images of a multilayer plain-woven fabric,[13] and Huang et al. proposed a novel framework that integrates μCT imaging and finite element methods to obtain an optimal mesh structure for simulation.[14] Recent advancements in artificial intelligence have facilitated the seamless integration of computer vision technologies into digital twins, enabling more precise classification, detection, and tracking of image objects.[15,16] The bottom–up approach, on the other hand, is implemented through data-driven 3D voxel modeling based on the material parameters of experimentally observed objects.[17–22] This approach generates virtual representations that are supported by top–down tomography identification. By adjusting the underlying statistical data, engineers can explore a wide range of voxel models and rapidly estimate material properties. These benefits create a practical environment for comparing new designs with existing models, enabling the derivation of optimized results. This concept was well addressed in recent papers reported by Lee et al., presenting two sequential processes, top–down and bottom–up digital twins, to create 3D microstructures of composite architectures. His group adopted a "top-down" approach, employing FIB-SEM to analyze the 3D microstructure of all-solid-state battery electrodes, thus uncovering the limitations of solid oxide electrolytes.[23] Additionally, they proposed a "bottom–up" approach at the electrode microstructure level of all-solid-state batteries, enabling electrochemical analysis and facilitating research and development.[24]

Despite the significant potential of this technique, most efforts have been narrowly focused on specific microstructures and did not extend to meso- and macro-structures across hierarchical length scales, where the volume of interest exceeds three orders of voxel length scale.[25–28] At such a limited scale, only the microstructural interactions between constituent elements can be effectively captured. Extending the analysis to hierarchical length scales allows for a more comprehensive examination of the relationships between microstructural interactions and macroscopic performance.[29,30] The digital twin driven by digital data holds significant potential for flexibly adjusting digital structures during hierarchical reconstructions across extensive length scales, surpassing traditional image-based models composed of static elements.

Recent interest has grown in voxel image modeling for designing large structures at coupon, element, component, and full-scale levels.[31–33] The biggest obstacle to applying them to macroscopic structures is resolution,[34–37] as the geometric quality and functionality are determined by the number of voxels. Digital twin models typically feature a single-scale geometric volume consisting of millions of voxels.[13,14] For sophisticated geometric configurations of macroscopic structures, more than 1 billion voxels must be filled in the image model volume, which poses a significant challenge for numerical simulation. Fortunately, the voxel model can be solved by the FFT (Fast Fourier Transform) numerical method, which enables high-precision interpretation while significantly reducing memory usage and computational costs, compared to conventional FEM (Finite Element Method) using tetragonal meshes.[38–40] Parallel computations on voxel meshes with regular size are 10–100 times faster than sequential computations on the same number of irregular tetragonal meshes with complex element-node connectivity. Modern graphics hardware with high computational power and massive parallelism has demonstrated the basic feasibility of processing giga-voxel models with high spatial resolution.[35,36] However, complex design representation remains difficult. Existing voxel drawing (handmade) and meshing (mesh to voxel), which are commonly used voxelization methods, either describe only coarse-resolution architectures or lack the compositional details needed to express hierarchical structures.[41] Furthermore, voxel drawing is a time-consuming process that requires drawing each object one by one, and voxel meshing relies on a resource-inefficient top–down process that divides a single feature model into appropriate unit voxels in one pass[42] (Figure S1, Supporting Information). Creating voxel-based complex objects without the extensive multiple-image data obtained from prohibitively expensive 3D scanning (scan to voxel) is highly challenging, and no mainstream method has been developed to efficiently distribute individual voxel units across massive volumes.[35,37] Since the first giga-voxel resolution case study on digital morphogenesis for linear elastic materials,[34] complex designs for anisotropic and nonlinear composite materials have not been attempted and are currently infeasible due to the lack of promising methods.

Herein, we present a novel digital twin strategy for designing multi-scale, giga-voxel digital models using a bottom–up assembly relationship, extending beyond the digital morphogenesis of anisotropic composite microstructures to include the hierarchical organization of mesoarchitecture. **Figure 1**a illustrates a systematic workflow for digital twin voxel modeling that interconnects 3D printing, computer vision, and tomography technologies. A closed-loop digital twin system integrating both top-down and bottom–up approaches was implemented to enhance model quality in three dimensions. This bidirectional framework established a synergistic closed-loop system, enabling feedback and synchronization between data and models for high-fidelity representation. Geometry-Find Al, driven by trained neural networks based on TensorFlow, characterized the anisotropic geometries within the tomographic microstructures of interest, resulting in a database of statistical geometric parameters and correlated physical properties (Figure 1b,c). Subsequently, data-driven image modeling mirrored a voxel-based digital unit twin of correlated anisotropic microstructures as building blocks, and a random seed process assigned each building block a unique identity. The generated building blocks, each comprising millions of voxels, were systematically expanded and assembled into 1D rows, 2D spaces, and 3D architectures to organize the bottom–up hierarchical configuration at giga-voxel resolution. The bottom–up manufacturing approach of the 3D printing process was similarly implemented in the assembly process, effectively serving as a digital 3D printing process to generate hierarchical and anisotropic configurations (Figure 1d). This hierarchical assembly model

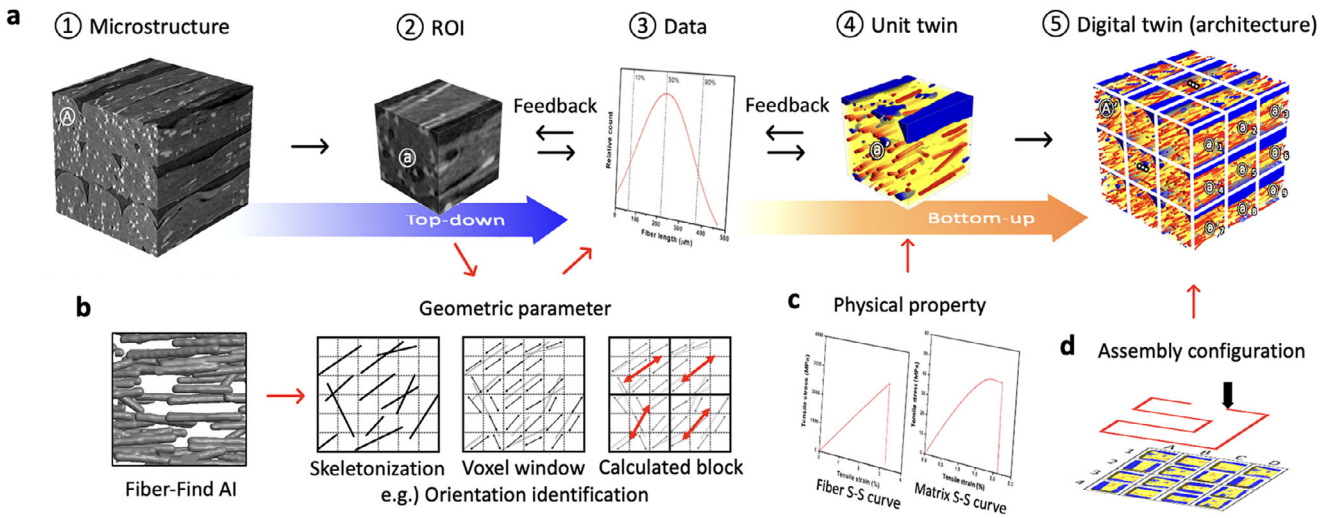

Figure 1. Overview of data-to-model closed-loop digital twin. a) Closed-loop digital twin workflow includes all procedures from tomographic analysis of microstructures to datafication of geometric parameters, and eventually to data-driven voxel modeling, as follows. ① Microstructure Ⓐ, ② region of interest (ROI) ⓐ, ③ data, ④ unit twin ⓐ', and ⑤ digital twin Ⓐ'. b) Computer vision-assisted tomography analysis using the trained Geometry-Find module. Individual geometries of constituent materials are accurately identified, enabling the extraction of statistical mother data for generating digital twins. c) Physical properties of constituent materials, obtained through experimental characterization, are recorded in a materials library and subsequently used to predict physical behavior. d) Assembly configuration was guided by the drawing path of the 3D printing process.

includes detailed information on both microstructure and macroscopic, spanning more than four orders of magnitude in length scale. Our digital twin workflow provides unparalleled capabilities for exploring the hierarchical and anisotropic nature of materials at multiple scales, including the orientation, distribution, and interactions of constituent components. The high-fidelity representation of the giga-voxel model, coupled with the fast computational speed of the FFT-heterogenization, demonstrated a powerful ability to identify microscale interfacial stresses between fibers and matrix in a comprehensive multiscale geometric volume.

2. Result

2.1. Data-Driven Digital Twin Voxel Modeling

The schematic process flow diagram shows the data-driven voxel modeling for a digital unit twin (**Figure 2**). This process generates a digital representation of the microstructure of interest derived from a statistical digital database obtained through experimental characterization, following steps: a. input image → b. data characterization → c. output image.

The input image (a) depicts the microstructure of a scanned sample of a 3D-printed composite architecture, where the periodic and hierarchical repeating unit volume is the region of interest. (We decided to adopt the FDM manufacturing method, a representative bottom–up process, as a material and process candidate for modeling the anisotropic microstructure architecture.) Individual-oriented filaments containing embedded fibers, bordered by weak interfacial voids, are identified as representative volumes for characterization. It is well known that nozzle jet 3D printing extrudes individual filaments to create complex alignment configurations (Figure S2 , Supporting Information).[43,44]

The intrinsic morphology and physical properties of its components determine the integrated properties of the material. The anisotropic microstructure is defined by the orientational and dispersive contributions of the fibrous material, highlighting the importance of accurately identifying individual fibers. To achieve precise fiber identification, Geometry-Find AI, driven by a U-net-based Neural Network, was employed, which had been trained to separate fibers from the surrounding matrix and identify isolated fibers (Figures S3 and S4, Supporting Information). Subsequently, a two-hidden-layer Artificial Neural Network (ANN)-based Fiber-Find AI analyzed fiber geometries for the segmented fiber objects (Figures S5 and S6, Supporting Information). As a result, all statistical fiber properties, such as diameter, length, orientation, and distribution of individual fibers, were quantitatively characterized.

(b. data characterization) In the data cloud, material information about the microstructure of interest-including geometric parameters (e.g., shape (R), length (l_f), volume fraction (V_c), orientation, and distribution (A_{ij})), physical properties (e.g., material type (s, l, g), basic physical properties (ν, α, E, G, K), and composite properties (σ_c, E_c, α_1, α_2))- is accumulated and informs a voxel generator to create high-resolution digital twins composed of micro-voxel grids (Figure S7, Supporting Information). The geometric information guides the spatial distribution of voxels to create the digital objects, while the physical properties are installed on each created object. As the material information expands by type, shape, and feature in the data cloud, the accuracy and diversity of digital representations improve.

(c. output image) The data-driven voxel modeling process creates the digital unit twin representations of the sub-volume structures with anisotropy attributes corresponding to each angular orientation of 0° ⓐ', 45° ⓑ', 90° ⓒ', and 135° ⓓ'. These sub-volumes are 0.5 mm-length cubes and are occupied with millions of voxels. The output results show that the unit twin of each

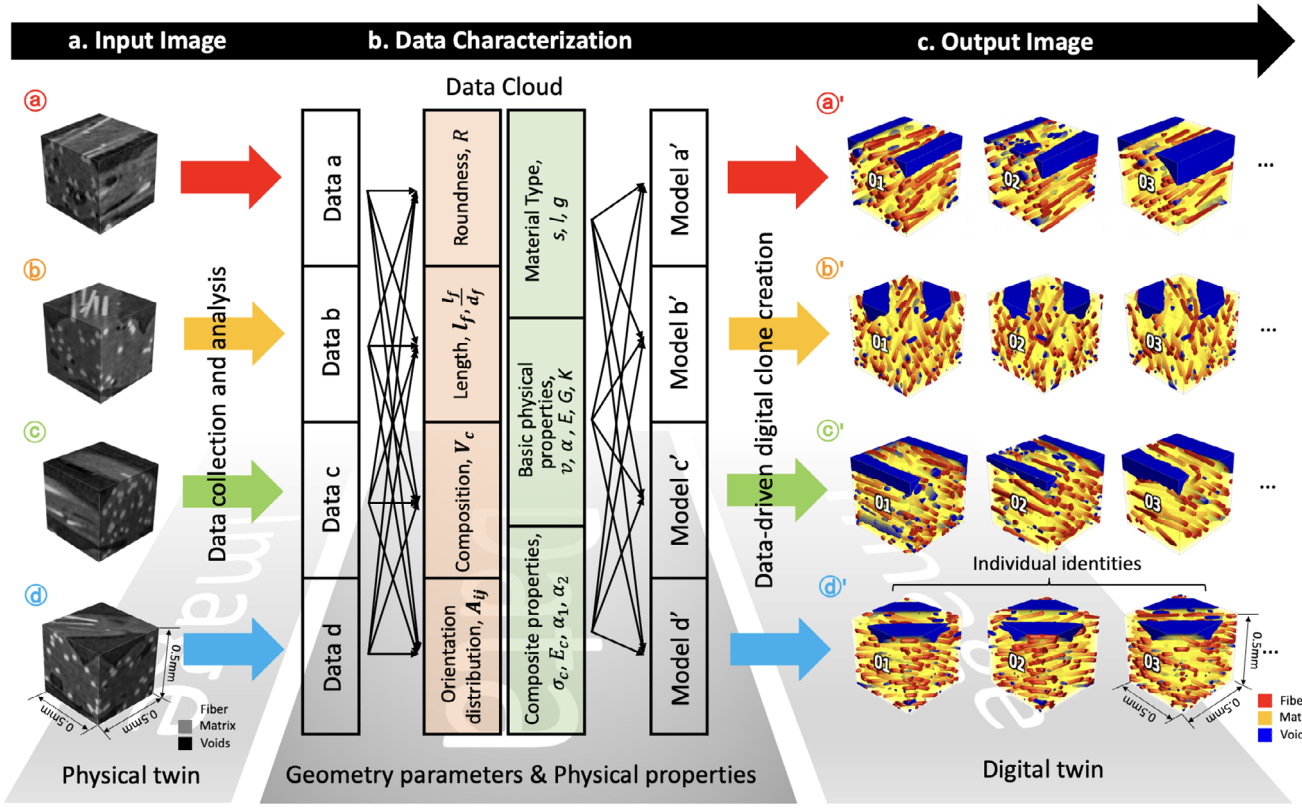

Figure 2. Data-driven digital unit twin voxel modeling. a–c) Voxel model generation through image-to-data and data-to-image transformations. (a) Input image. The tomographic microstructures of 3D-printed composite materials. The region of interest was a periodic and hierarchical repeating unit volume (size 0.5×0.5×0.5 mm^3). Four anisotropic microstructures corresponding to the orientations of ⓐ 0°, ⓑ 45°, ⓒ 90° and ⓓ 135° were prepared. (b) Data characterization. Geometrical parameters and physical properties are experimentally characterized and converted into a statistical digital database. (c) Output image. The data-driven voxel model generator created the digital unit twins of the sub-volume microstructures, corresponding to each angular orientation: ⓐ' 0°, ⓑ' 45°, ⓒ' 90° and ⓓ' 135°. The random seed generation process assigns unique identities to the unit twins, establishing a one-to-many relationship.

oriented block satisfies a high-fidelity virtual representation in terms of both external and internal geometries. In our study, we considered four representative fiber orientations for simple verification. The greater the diversity of orientation blocks, the more diverse anisotropic mesostructures can be generated. As a side note, we declare that this study uses the voxel generator, a geometry generation module developed by Math2Market GmbH, that can generate multiple voxel geometry models associated with different geometric parameters. Strictly speaking, these voxel models are synthetically generated geometry models based on given data, through predefined computer algorithms. The voxel generator allows users to efficiently generate a large number of digital prototypes based on simple data alterations in the shortest possible time (Figure S8, Supporting Information).

Traditional computer-aided engineering (CAE) modeling methods are largely unsuitable for generating precise mesostructural models due to the inherent challenges of representing the vast number and complexity of flexible micro-elements[45,46] (Figure S9, Supporting Information). These models normally consist of static elements, limiting their adaptability to design variations. Data-driven digital twin process features bidirectional synchronization between digital and physical twins, which facilitates immediate dynamic adjustments (short-term dynamics), sequential design modifications, and reverse engineering (long-term dynamics). These capabilities help bridge the gap between digital models and physical outputs. A concise overview of the advantages of data-driven modeling for dynamic models compared to traditional static models is provided in (Figure S10, Supporting Information). The smallest repeating unit cell in mesoscale models, known as the Representative Volume Element (RVE), is defined as a digital unit twin volume ⓐ, representing the entire material Ⓐ. Here, RVE volume was defined as a single repeating unit cell that represents simple anisotropic microstructures while also serving as a building block for assembly elements. Since the 3D printer extrudes material using a 0.5 mm nozzle, a cubic volume of 0.5 × 0.5 × 0.5 mm^3 was determined as the RVE volume. When a large number of reconstruction models from samples are available, RVEs can provide substantial amounts of raw data that satisfy the relationship $F(A) = mean\, f(a)$. However, these models still cannot fully account for the variability of their physical twins due to their basis in static model images. On the other hand, a digital twin creates a virtual representation of a sub-volume structure through data-driven voxel modeling, enabling the creation of near-innumerable digital unit twins ⓐ' digitally copied from the variable digital data about the unit volume ⓐ. Note that the digital unit twin ⓐ' is different from the sample

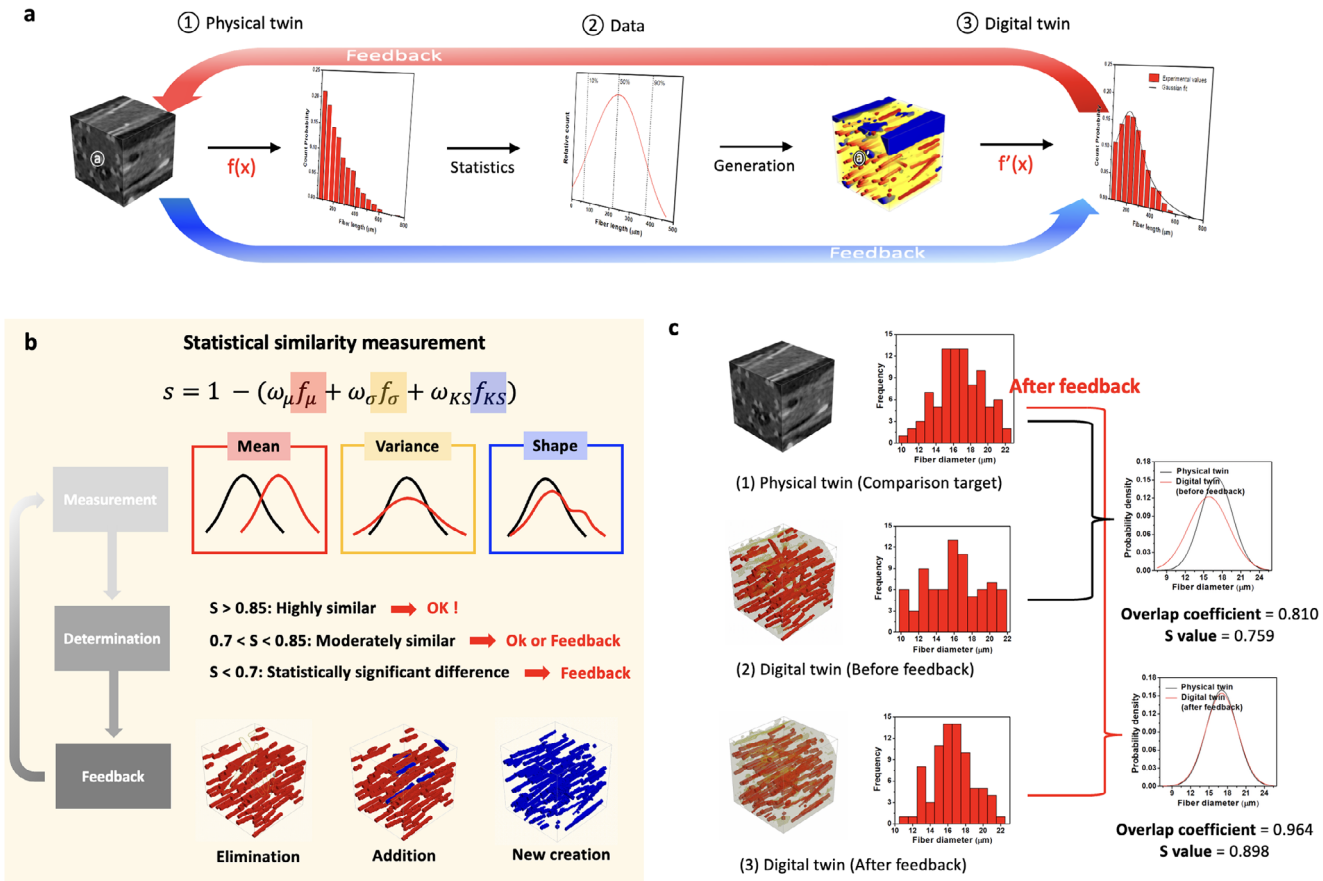

Figure 3. Closed-loop feedback mechanism between the physical twin and the digital twin. a) The core feedback mechanism is applied to the building-block model generation process, which performs image-to-data and data-to-image transformations. b) Statistical similarity measurement compares the mean (f_μ), standard deviation (f_σ), and dispersive shape (f_{ks}) between two statistical curves derived from the physical domain and the digital model. The similarity index, S, consisting of these three comparison terms, serves as a metric to determine whether feedback should be applied. Here, ω denotes a weighting function that allows adjustment of the S-value according to specific objectives. If a low S value is recorded, the initial model is modified to better approximate the physical domain based on the three statistical comparison terms. The modification process can be done by using a voxel model generator to correct or remove erroneous objects, generate additional objects, or ultimately generate a new digital twin model. c) Example of a feedback application. Statistical data corresponding to the left image model are prepared. The overlap coefficient and S-value between the two Gaussian-fitted statistical curves are computed to determine whether feedback is needed. After feedback, the S-value improves from 0.76 to greater than 0.85, indicating enhanced similarity between the physical and digital domains.

volume ⓐ as it is an infinitely copiable digital model with an individual identity assigned by a random seed process (i.e., one-to-many relationship). Randomness is introduced into the model through a random seed process, which assigns a unique number to each generated model (Figure S11, Supporting Information). This process enables the generation of new microstructures by comparing them to previously generated microstructures. Simultaneously, this process ensures the physical validity of the generated models by balancing structural similarity to physical twins with the flexibility required for design variability (Table S1, Supporting Information). That is, this random seed generation offers a high degree of design flexibility, assigning unique identities to the digital unit twins ⓐ' (Figure S12). Consequently, with a large data cloud for the unit volume ⓐ, the entire material property can achieve an ideal structure-property relationship such that mean f(a) = mean f(a'). This indicates a high degree of design freedom based on extensive data.

2.2. Closed-Loop Feedback Mechanism

Our digital twin workflow adopts both image-to-data and data-to-image transformation pipelines. Notably, the structured numerical data produced during this process offers unique flexibility in design modifications, especially when compared to unstructured voxelized images. Since model generation is fundamentally data-driven, the design space for microstructural architectures can be significantly expanded depending on the diversity and richness of the parameterized datasets available. This data-centric approach not only supports detailed geometric representation but also enables extensive structural exploration, rapid property prediction, and even inverse optimization.

The feedback mechanism is designed to operate within the building-block generation process, which performs both image-to-data and data-to-image conversions (**Figure** 3a). Microstructural information obtained from the physical domain is

accumulated and statistically quantified. These statistical parameters not only serve as input for generating digital models but also act as criteria for determining whether feedback should be applied to improve model fidelity.

To this end, we introduced a similarity metric, denoted as **S**, comprising three statistical components—mean, variance, and dispersive shape (Figure 3b). The S-value quantifies the discrepancy between statistical curves derived from the physical and digital twins. If a low S value is recorded, the initial model is modified to better approximate the physical domain based on the measured mean, variance, and dispersive shape information. Modifications can be done by using a voxel model generator to correct or remove erroneous objects, generate additional objects, or ultimately generate a new digital twin model. Figure 3c illustrates an example of this feedback application. Microstructural parameters extracted from the image model were first converted into statistical data. The overlap coefficient and S-value between two Gaussian-fitted distributions were computed to determine whether feedback was required. After feedback was applied, the S-value improved from 0.76 to over 0.85, indicating enhanced statistical similarity between the physical and digital twins. The feedback mechanism is not limited to a specific set of parameters but can be applied to any measurable geometric parameter involved in model generation (Figure S13, Supporting Information). For each parameter, the feedback evaluation can be flexibly customized by adjusting the weighting functions assigned to the mean, variance, and distributional shape components.

Ultimately, to ensure the mechanical relevance of the generated model to the physical domain, the predicted mechanical strength was compared against experimental measurements (Figure S14, Supporting Information). Importantly, this validation is not a one-time process. Rather, the model's output can be iteratively refined through the data-driven feedback loop, allowing for systematic updates and enhanced mechanical reliability via quantitative comparison with experimental results.

2.3. Digital Assembly of Hierarchical and Anisotropic Architectures

Our modeling approach enables a full-scale exploration of structural anisotropies within a broader and more comprehensive framework. We consider digital unit twins not only as representations of anisotropic microstructures but also as subvolumes belonging to hierarchical and anisotropic structures. The digital assembly process extends the model volume by integrating digital unit twins of cubic volumes onto each of the six sides of ±X, ±Y, and ±Z axes (Figure 4a-c). In this process, each individual volume ⓐ′$_1$, ⓐ′$_2$, ⓐ′$_3$. ⓐ′$_n$ of the unit twins serves as a fundamental building block for constructing the digital architecture Ⓐ′. Module blocks α', β', and γ' are defined as a grouping of pre-attached building blocks ⓐ′$_n$. Module blocks composed of multiple unit twins at different scales can also be implemented (Figure S15, Supporting Information). Complex parts requiring detailed descriptions can be composed of smaller unit cell sizes, while rougher parts can be composed of larger unit cell sizes.

The output properties F'(x) of the assembly Ⓐ' depend on the global average of the individual properties f'$_n$(x) of these building blocks ⓐ′$_n$. When extended to the meso-length scale, the voxel volume hierarchically forms the exterior shape of the object while preserving the microstructural identity of the individual unit volumes. This process initially arranges the basic building blocks in 1D rows, expands them into 2D space, and eventually stacks them into a 3D architecture. One-to-many relationship (where a single physical domain corresponds to multiple digital unit twins) enables the creation of a building block continuum with diverse structural profiles. The key factor in controlling consistency was maintaining a continuous orientation alignment on a hierarchical scale. To achieve this, the building blocks were connected parallel to their orientation, avoiding perpendicular connections. This ensured a seamless assembly and alignment of the microstructural components.

A series of bottom–up modeling workflows demonstrates the digitally created digital twins of both the single building block and the digital architecture, compared to the real-world samples (Figure S16, Supporting Information). Statistical analysis results from the two different scales of digital twins (building block and architecture models) revealed strong structural similarities with the physical domain. The analysis of variance (ANOVA) also demonstrated no significant mean difference among the three groups (1-experimental, 2-building block, 3-architecture) with a p-value > 0.05, thus supporting each other's results well (Table S2, Supporting Information). These results suggest the feasibility of extending this concept using a bottom–up approach. The bottom–up approach to mesoscale modeling demonstrates the capability to simplify and hierarchize complex systems across multiple scales of interest.

Figure 4d–g presents a straightforward strategy for digital assembly by stacking sequences using module blocks. When unit cell structures are repeated at large length scales, the tedious process of stacking can be significantly reduced by grouping volume domains with the same structures or functions into independent module units. In this study, we performed data characterization and digital twin for layered structures of 3D-printed short-fiber reinforced composites that exhibit structural hierarchy according to the stacking sequence.

The layered structure of the real sample consists of stacking layers with orientations of ⓐ 0°, ⓑ 45°, ⓒ 90°, and ⓓ 135°, where each layer was hierarchically stacked with a 45° raster angle. Accordingly, the digital models consist of the building blocks with digital representations of ⓐ' 0°, ⓑ' 45°, ⓒ' 90°, and ⓓ' 135° orientations, respectively (Figure 4d,e).

Next, digital assembly by stacking sequences of module blocks was performed (Figure S17, Supporting Information). The detailed assembly process proceeded in the following order: (1) 2D space expansion (modulization), and (2) 3D layer stacking (stacking sequence). The following 4 sets of 2D layers made up of unit twins were prepared first: A'={a'$_1$, a'$_2$...a'$_{16}$}, B'={b'$_1$, b'$_2$...b'$_{16}$}, C'={c'$_1$, c'$_2$...c″$_{16}$}, D″={d″$_1$, d″$_2$...d'$_{16}$}.

These 4 sets of 2D layers are assigned to module blocks, named Ⓐ', Ⓑ', Ⓒ', and Ⓓ'. Then, the module blocks were digitally stacked in the following order:$[A'/B'/C'/D'/A'/B'/C'/D']_{heli}$

This layered structure represents a helicoidal stacking sequence, showing a hierarchical microstructure (Figure 4f). By adjusting the stacking layer orientations, quasi-isotropic (QI) architectures can be reconstructed digitally (Figure 4g). The stacking orientation information for the QI architectures is as follows:$[0°/90°/45°/135°/135°/45°/90°/0°]_{QI}$

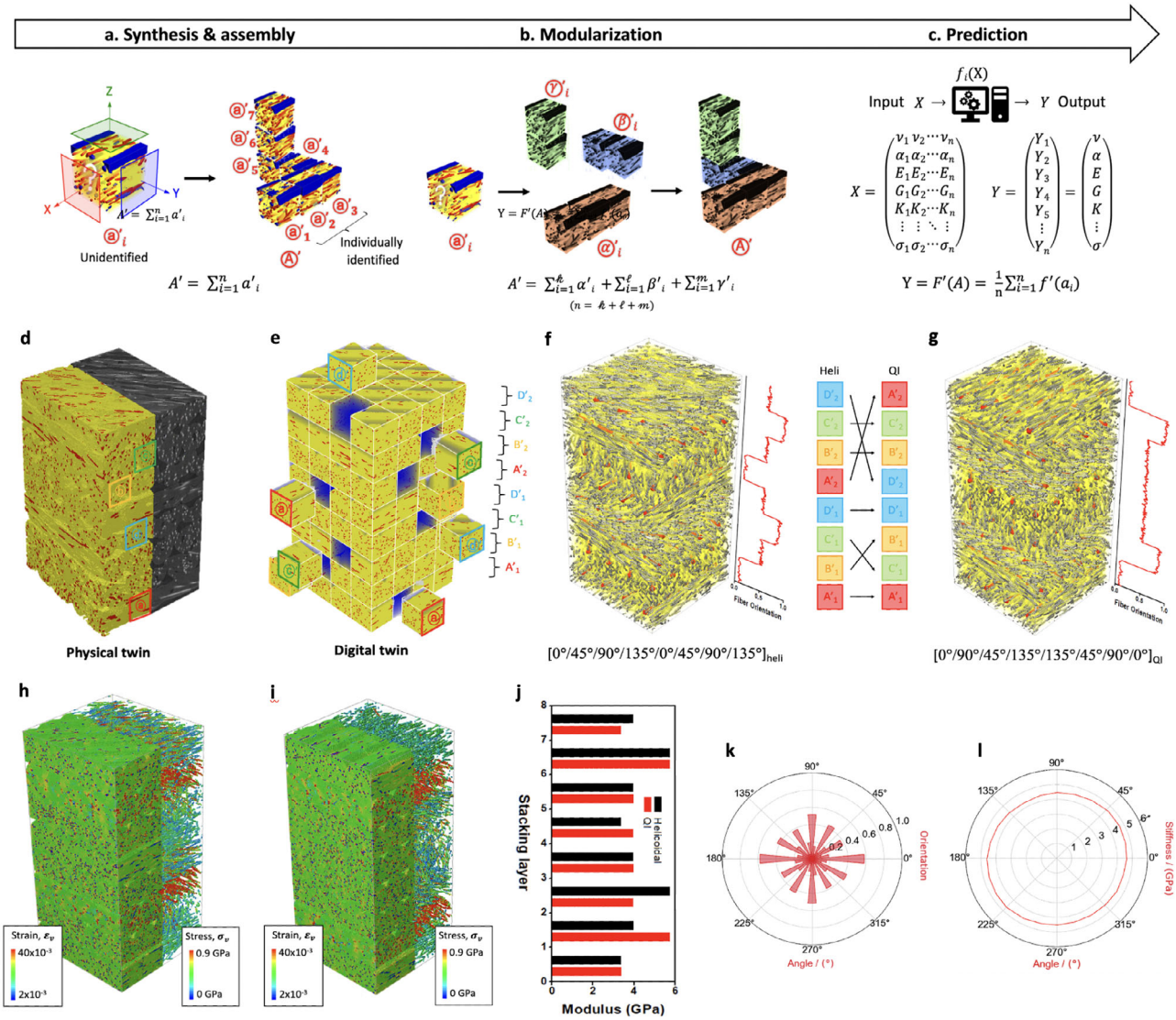

Figure 4. Digital assembly of hierarchical and anisotropic architectures. a,b) Digital assembly is the process of expanding unit blocks of individual identities to the mesoscale. (a) Digital synthesis is the intermediate process of building small-scale groups, and (b) the resulting blocks are defined as module blocks that can be assembled into larger-scale architectures. c) Output properties depend on the global average of the individual properties of the building blocks. d) Reconstructed physical twin model of μCT scanned tomography of 3D-printed hierarchical layered composites. The marked regions are the equivalent unit volumes of ⓐ 0°, ⓑ 45°, ⓒ 90°, and ⓓ 135° layers. e) Digital twin model consisting of the building blocks of the ⓐ' 0°, ⓑ' 45°, ⓒ' 90°, and ⓓ'135° orientations. f,g) Stacking sequence orientations for Helicoidal and quasi-isotropy (QI) layer configurations. Red arrows indicate the fiber orientation in individual building blocks. h, i) Von Mises strain (left)/Stress (right) of Helicoidal and QI digital twin models in tensile mode. (loading direction = 90°) j) Comparison of modulus-stacking layer profiles in Helicoidal and QI digital twin models. k, l) Global orientation and modulus of Helicoidal and QI digital twin models for each azimuth angle in the *X*–*Y* plane.

Depending on the stacking sequence, the fiber orientation, modulus, and anisotropic characteristics of the digital architecture were modified layer by layer, resulting in gradual helical curves turning into symmetrical curves as shown in Figure 4f–j. In contrast, the spherical graphs in Figure 4k,l show that the global-scale calculations of fiber orientation and modulus are isotropic in both stacking orientations. Since the same module blocks were used, but only the stacking order was different, the global approaches yielded the same results. The above result directly demonstrates the scaling effect from local (anisotropy) to global (isotropy) in the physical properties of hierarchical composite materials at multiscale, compared to locally and globally Isotropic configurations (Figure S18, Supporting Information).

2.4. Integrative Approaches for In-Plane Anisotropic Configurations

The above sections have focused on cases of uniform in-plane orientations. Here, we extend our attention to new strategies for

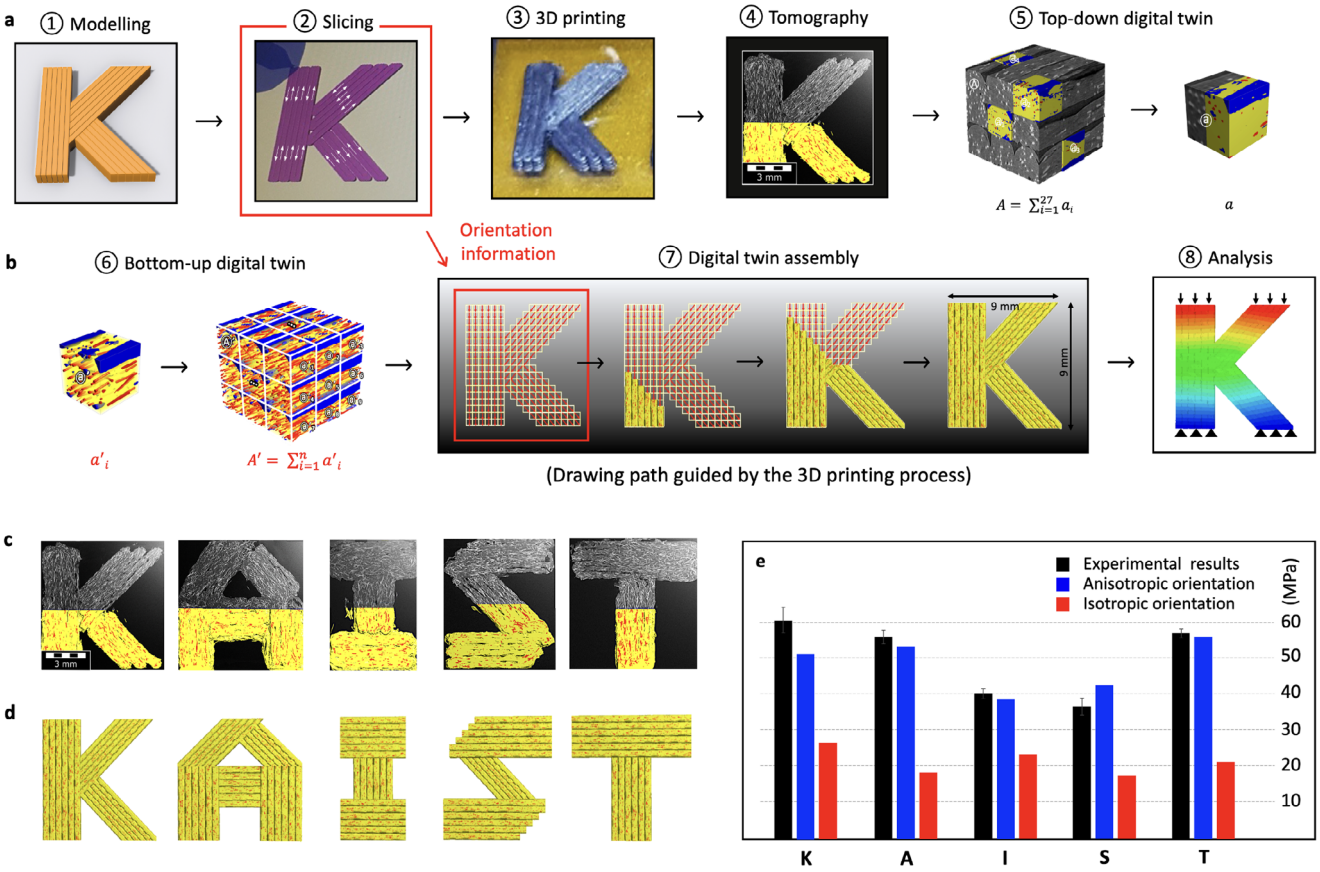

Figure 5. Integrative approaches for in-plane anisotropic configurations. The bottom–up and top–down approaches are comprehensively extended to all processes, including sample fabrication, modeling, and analysis. a) Top–down digital twin process; ① initial modeling, ② slicing, ③ 3D printing, ④ tomography, ⑤ digital twin. b) Bottom–up digital twin process; ⑥ data-driven unit twin modeling, ⑦ digital twin assembly, ⑧ analysis. Note that the drawing path during the slicing and printing process determines the orientation configuration of the meso-architecture and provides data about in-plane orientation for the digital assembly process. c) Tomographic images (2D sections) of anisotropic text-character architectures as physical twins. The maximum compressive strength was obtained experimentally. d) Digital twin models of text-character architectures with anisotropic fiber orientation. The fiber orientation is parallel to the printing direction along the text outline. e) Comparison of maximum compressive strength of physical/digital twins and anisotropic/isotropic text-character architectures.

describing complex planar orientations. When the in-plane orientation is intricate, additional efforts are required to extract the corresponding information from the microstructure. This challenge can be addressed using top–down and bottom–up digital twin processes. **Figure 5** illustrates the sequential process of digital twin creation using both top–down and bottom–up modeling approaches. The top–down digital twin, depicted in Figure 5a, models and characterizes the RVE volume for the region of interest based on precise tomography images. Conversely, the bottom–up digital twin, shown in Figure 5b, employs data-driven modeling to create a digital twin from a database of material characterizations. These top–down and bottom–up approaches can also be extended to all processes, including sample manufacturing, modeling, and analysis. In the top–down process, sample manufacturing follows a sequential procedure of initial modeling, slicing, and 3D printing. Similarly, the bottom–up process involves digital assembly to create a meso-architecture by replicating the architectural concepts of the 3D printing process. It is important to note that the drawing path during the slicing and printing process determines the orientation configuration of the meso-architecture and provides in-plane orientation data for the digital assembly process (Figure S19, i.e., the assembly relationships are derived, Supporting Information). This suggests that digital twin and printing processes can interact synergistically to facilitate 3D digital assembly. The high degree of design freedom enabled by the 3D printing process offers significant advantages for designing in-plane orientations. These proto-drawings do not need to be limited to 3D printing but can originate from any method that provides assembly relationships.

Figure 5c,d illustrates the anisotropies in the physical and digital twins of the text-character architectures. Five text characters were prepared in a geometric volume of $9 \times 9 \times 1.5$ mm^3 for this study: "K," "A," "I," "S," and "T." The K-character features an anisotropic geometry with a vertical column and a brace supporting a 45° sloping beam, while the A-character represents a strut-tie structure. The I- and T-characters exhibit bi-symmetric stable structures with short and long vertical columns, respectively, and the S-character displays a radial symmetric structure with a sloping central column. Although slight dimension offsets were observed in the tomography images, the digital twins

and physical twins showed significant similarities in external geometry. The digital twins demonstrate robust structural integrity as a continuum of building blocks, whereas the physical twins exhibit minor dimension irregularities induced by the FDM process. These deviations, while inevitable, did not compromise the overall structural representation.

The infill patterns of the text-characters show anisotropy, characterized by highly aligned subfilament bundles along the programmed process direction (rows 1 in Figures S20 and S21, Supporting Information). The internal fiber orientation/distribution in the digital twins (row 2 in Figure S20, Supporting Information) also closely matches the characterized fiber orientation information in the reconstruction models (row 2 in Figure S21, Supporting Information). The modulus plot over 360° in the main XY plane effectively shows the process-induced planar orientation along the contour shape of the text characters, and consequently derives the anisotropy A_E defined as the max-to-min modulus ratio (row 6 in Figure S21, Supporting Information). Notably, the K- and S-characters exhibit high elastic anisotropy due to the high partiality in the fiber orientation. However, the experimental strain fields exhibit trends broadly consistent with simulation results, albeit with some residual symmetry (e.g., in the A and T-characters), likely caused by geometric imperfections introduced during the printing process. These dimensional inconsistencies at the assembly level highlight the potential of data-driven feedback mechanisms to correct such deviations and enhance model fidelity (Figure S22, Supporting Information). This potential allows the proposed bottom–up digital twin to not only provide high-fidelity representation and scalability, but also enable extensive structural exploration, rapid prediction, and even inverse optimization. Existing scan-to-voxel approach remains a critical pathway for mesoscale structural modeling, enabling the transformation of high-resolution scan images into precise digital models suitable for parametric analysis. However, such models are inherently limited in design flexibility. They are typically constrained to one-time analyses and allow only minimal editing, making them unsuitable for iterative design exploration. In contrast, the data-based feedback mechanism provides inherent flexibility for model modification, overcoming the limitations of fixed scan image models and supporting broader design adaptability.

The maximum compressive strength of the anisotropic samples was compared with that of the text characters of isotropic infill patterns (Figure 5e; Figure S23 , Supporting Information). Among the general trends of high strength in anisotropic samples, the A-character shows almost 2.5 times higher maximum compressive strength in the anisotropic infill patterns due to efficient load transfer by the load-direction fibers, along with a stable geometric shape. These anisotropic behaviors of composite text characters expand our interest from material mechanics to composite mechanics. Until now, most of the interest has been limited to the external geometries of struts and nodes,[26,27] especially focusing on infinite periodic structural materials, such as auxetic metamaterials[47–49] and cellular architectures,[50] which consist of either single symmetric or multiple asymmetric unit cells. To facilitate approximate design, the repeating unit cells have been simplified into isotropic single-phase materials[51,52] or given an effective value to characterize the anisotropic properties.[53,54] Although this simplification is an efficient strategy for mesostructured design, it often results in the loss of critical microstructural details, leading to a potentially inaccurate representation of the actual structure. In contrast, composite structures have very complex internal microstructures, showing various shapes, diameters, lengths, contents, orientations, and distribution characteristics of fibers embedded inside, which are distinct from the flat and pure microstructures of single-phase materials. These fiber characteristics significantly affect the small and large deformation behaviors of the composite structure, and therefore, their relationship must be thoroughly understood.

2.5. Giga-Voxel, Full-Scale Digital Twin Meso-Architectures

High-fidelity micro-building blocks were eventually utilized for digital assembly in a specific layup configuration, with distinct orientations for each layer. This work is particularly challenging due to the structural complexity in both planar orientation and stacking sequence. However, the proposed strategy can effectively address these challenges. As an illustrative example, a 3D "castle" sample of substantial giga-voxel architecture ($40 \times 32 \times 12$ mm^3) was designed, and the results are shown in **Figure 6**. Giga-voxel means the number of voxels occupying a volumetric space of a large structure, rather than focusing exclusively on the smallest individual voxel unit. For modeling of large structures, a key decision involves defining both the resolution of a single voxel and the overall size of the structure. To occupy the massive volume of castle architecture while expressing fine-sized fibers simultaneously, a giga-scale number of voxels with a 4-micron resolution should be prepared (Figure 6a–c). A coarse voxel size of 16 microns or more is insufficient to accurately represent individual fibers with smaller diameters and lengths, leading to the loss of orientation information and a diminished stiffness enhancement effect (see Figure 6d,f,g).

The following describes the giga-voxel modeling procedure for the castle architecture. To systematically design the internal microstructure in all layers, the drawing path of the printer nozzle was pre-explored and adjusted for each layer using the slicing software before fabricating the samples (Figure S24, Supporting Information). In this design, six drawing paths were prepared for 64 stacking layers along the Y axis. During the actual fabrication process, the castle sample was printed in a planar orientation guided by the drawing path for each layer. Accordingly, in the digital twin process, the type and arrangement of the building blocks in individual layers were matched precisely with the drawing path in the printing process. More than ten thousand building blocks, each consisting of millions of voxels, were prepared for the structure and were ultimately stacked to form a 3D giga-voxel structure. This structure contains an immense number of oriented fibers, amounting to millions (Figure 6e,f). The orientation and distribution of the fibers are determined block-by-block by the unit twin generator, and thus, the arrangement and assembly of the building blocks systematically distribute millions of fibers in giga-voxel space. However, using a giga-voxel model with billions of degrees of freedom for numerical simulations requires massive computational resources. This computational cost was efficiently managed with a 40% acceleration by using composite voxels, which are created by merging multiple voxels (4×4×4) into a single voxel (Figure S25, Supporting Information). When using

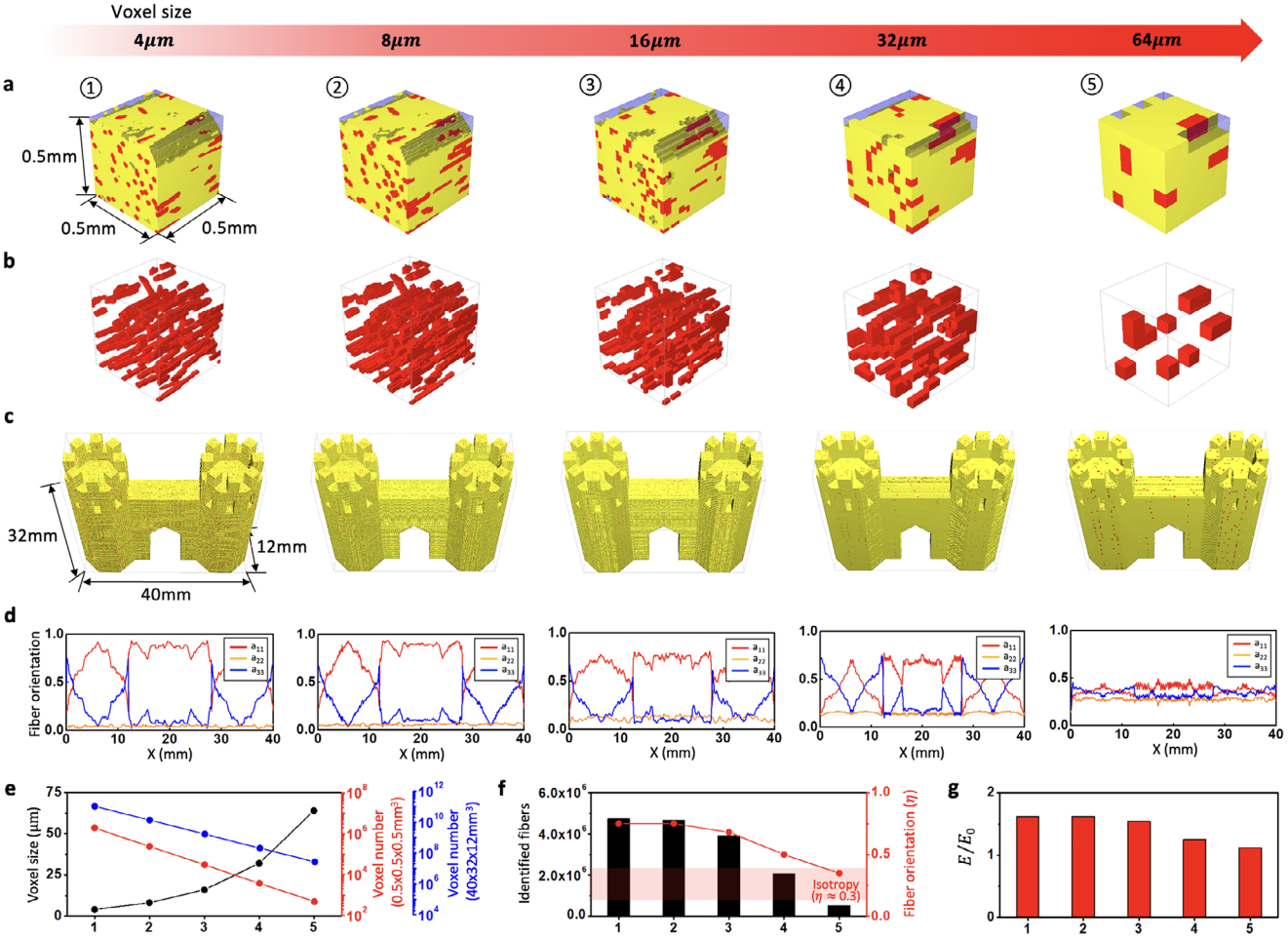

Figure 6. Geometric relationship between voxel size and giga-voxel model. a) A set of unit building blocks with a volume size of 0.5 × 0.5 × 0.5mm^3 in increasing order of voxel size. b) Voxel geometry changes of embedded fibers (red) according to voxel size. Voxel sizes smaller than fiber diameter and length fail to accurately describe the individual distributed fibers (fiber diameter = 15 μm, fiber length = 100 μm). Voxel sizes of 32 and 64 μm show rough aggregate fiber geometries. c) Giga-voxel models occupying a volume size of 40 × 32 × 12 mm^3. As the voxel size increases, the geometry surface becomes rougher. d) Fiber orientation profiles showing internal microstructural information. At low voxel sizes, the upper and lower curves of the principal orientation tensors a_{11}, a_{33} show a high degree of fiber orientation, indicating an anisotropic system. As the voxel size increases, the curves of the principal orientation tensors a_{11}, a_{22}, a_{33} become closer together, indicating a loss of orientation information. e) Number of voxels that occupy the building blocks and castle assemblies, depending on the voxel size. Building blocks of millions of voxels reach giga-voxels when prepared in tens of thousands. f, g) Number of identified fibers and their contribution to the stiffness enhancement. A hundred fibers in one block form millions of distributed fibers in a giga-voxel model. Failure to identify fibers leads to low anisotropy and low stiffness enhancement.

composite voxels, the composite properties are computed based on the laminate theory, and then direction-dependent properties are represented correctly. Furthermore, the FFT numerical solver method synergistically combines high-speed parallel computation with precise local analysis capabilities in voxel-based models. As a result, we successfully solved the giga-voxel model in less than a single day with a multiple-core parallelization process, as opposed to a week or longer with conventional methods (Table S3, Supporting Information).

The resulting digital assembly not only retains detailed microstructure at micro-voxel resolution but also exhibits a sophisticated exterior in three dimensions at giga-voxel volume scale (**Figure** 7a). As the number of voxels increases from 10^6 (mega) to 10^9 (giga), the digital model represents all individual fibers, building blocks, local features, and the full structure at multi-scales from 10^{-3} (micro) to 10^1 (macro) length-sizes. Consequently, the 3D graphs of microstructural information display the fiber orientation/distribution and mechanical modulus variation along the *X*, *Y*, and *Z* axes (Figures S26 and S27, Supporting Information). The prototype model, printed castle, and its tomographic observation (×0.4) are externally very similar to the digital twin model, but they do not provide detailed information about the internal microstructure. Obtaining a multiscale tomography of this sample requires multiple scans due to the trade-off between voxel resolution and field-of-view. The horizontally cropped plane images show that the bottom–up model contains detailed fiber orientation information, which matches the drawing path in the slicing process and orientation analysis results (Figure S28, Supporting Information). As a result, the fiber orientation/distribution of the macro castle model across the Y axis

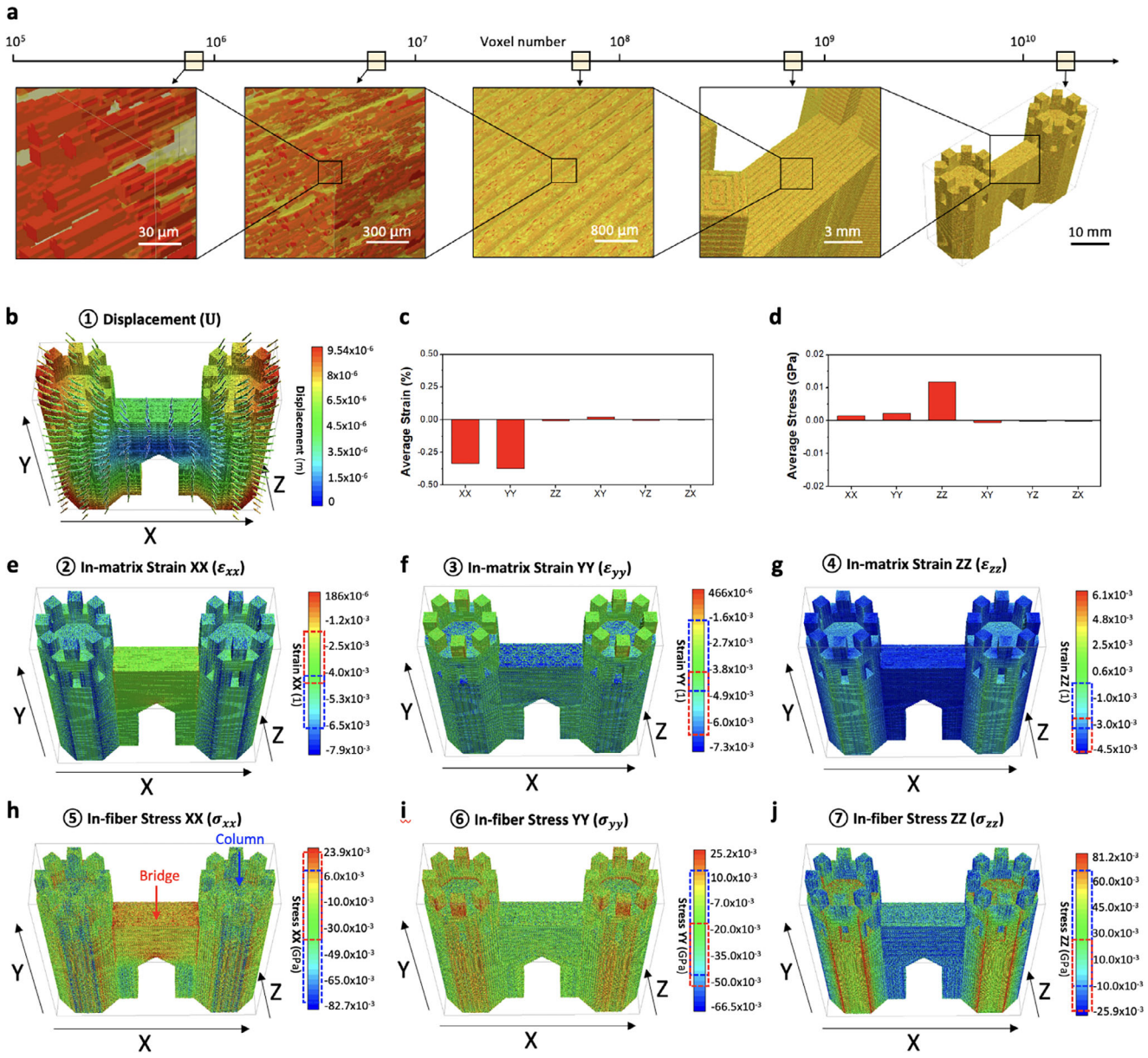

Figure 7. Hierarchical assembly of giga-voxel, multi-scale castle architecture. a) Giga-voxel, multi-scale digital twin encapsulating from digital morphogenesis of anisotropic microstructures to hierarchical assembly of meso-architecture. More than ten thousand building blocks, each consisting of millions of voxels, were prepared and systematically stacked to form a 3D giga-voxel architecture. This structure contains 10 million oriented fibers, tailored to reflect the intended anisotropic configuration. b–e) Displacement, strain, and stress maps showing the degree of shape shrinkage, local deformation, and stress concentration in three dimensions. b) Displacement (*U*) showing the 3D load directions determined by the thermal history (50 °C → RT). c,d) Negative values of average strain resulted from thermal shrinkage and correlated stress values. e–g) In-matrix strains XX (ε_{xx}), YY (ε_{yy}), and ZZ (ε_{zz}) responding to 3D shrinkage directions. h–j) In-fiber stresses XX (σ_{xx}), YY (σ_{yy}), and ZZ (σ_{zz}) responding to 3D shrinkage directions. The red and blue checked areas in the histogram represent the stress or strain scale range for the bridge and column areas, respectively.

was quantified in the graphs (Figure S29, Supporting Information). The six in-plane orientations clearly show high intensities and distinctive orientation variations in the X and Z directions, represented by a_{11} and a_{33}, respectively.

Due to hierarchical construction, 3D-printed architectural models exhibit varying degrees of infill density and anisotropy in different localized regions, which affects the anisotropy of thermal expansion and shrinkage, resulting in geometric errors in three dimensions. Using multiphysics simulation, the dimensional errors of the initial design post-solidification (50 °C → RT) during the real-world fabrication process were investigated on the digital twin (Figure 7b–j). The displacement, strain, and stress maps in Figure S30 (Supporting Information) display the degree of shape shrinkage and local strain, and stress concentration in three dimensions, respectively. The in-fiber and in-matrix strain and stress maps shown in Figure 6e–j, Figures S31 and S32

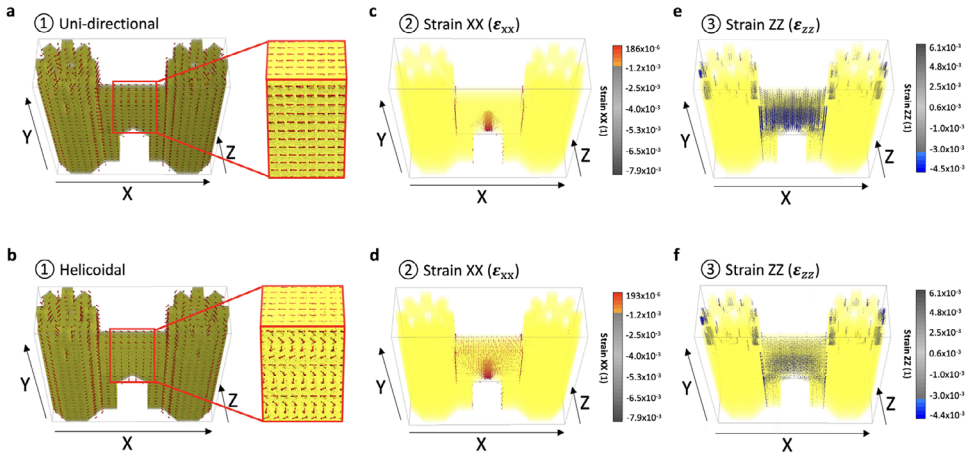

Figure 8. Interfacial micro-level thermal stress concentrations in mesoscale architectures with unidirectional and helicoidal configurations. a, b) Computed fiber orientations across the castle models. Red arrows in the expanded region indicate (a) unidirectional and (b) helicoidal configurations in the bridge region. c, d) Map results of ε_{xx} (for $\varepsilon_{xx} \geq -1.2 \times 10^{-3}$) show that the mechanical restraint of the longitudinal fibers in (c) the unidirectional configuration significantly suppresses the thermal strain in the bridge region compared to (d) the helicoidal configuration. e, f) Map results of ε_{zz} (for $\varepsilon_{zz} \leq -3 \times 10^{-3}$) show that (e) the unidirectional configuration suffers from more severe thermal strain in the bridge region than (f) the helicoidal configuration. A comparison of the ε_{xx} and ε_{zz} maps reveals that the unidirectional configuration exhibits high thermal stress anisotropy ($\varepsilon_{xx} << \varepsilon_{zz}$), whereas the helicoidal configuration shows relatively less thermal stress anisotropy.

(Supporting Information) capture the stress transfer from the matrix to the fibers. Due to its anisotropic geometry, the bridge region exhibited significant anisotropy in thermal strain and stress between the X and Z axes. In particular, the value of ε_{zz} was prominent in the bridge region where the fiber orientation was perpendicular to the Z axis. In this case, the mechanical restraint effect of the fibers is reduced (note the relatively low stress σ_{zz} between the fiber-matrix interface), approaching the TCE of the matrix material. The stress and strain profiles shown in Figures S33 and S34 (Supporting Information) numerically quantified the magnitude and variation of the stress and strain distributions in the fibers and matrix across the bridge and column regions.

The orientation and ε_{zz} maps, shown in **Figure 8**, demonstrate that the helicoidal configuration mitigates the anisotropy of thermal shrinkage compared to the unidirectional configuration. The distinctive orientation fingerprints determined by the unidirectional and helicoidal configurations in the range of X = 12–28 mm are compared (Figure S35, Supporting Information). When the bridge region is unidirectional, all layers exhibit high negative ε_{zz} values due to the transverse orientation of the fibers. In contrast, the helicoidal configuration, by balancing layer orientations, forms a globally isotropic system, resulting in a relatively low strain field. Experimental verification was also done to measure the dimensional size changes of the unidirectional and helicoidal samples before and after thermal history, and the measurements slightly supported the simulation outcomes, indicating that the helicoidal configuration exhibits less anisotropy in thermal shrinkage (ΔL) (Figures S36 and S37, Supporting Information). Overall, we demonstrated that the digital twin, incorporating both extrinsic and microstructural information, effectively captures thermal shrinkage behavior influenced by both the microstructure and the extrinsic model across a comprehensive multiscale length scale.

3. Conclusion

We leveraged 3D tomography, computer vision, AI, and data-driven voxel image modeling to build a closed-loop digital twin that interconnects structured (data) and unstructured (image) information. The core contribution of this study lies in the seamless integration of both top–down and bottom–up voxel modeling approaches within a unified digital twin pipeline. This hybrid methodology not only ensures high-fidelity representation and scalability but also enables genuine design adaptability. By bridging parametric data generation, voxel-based model construction, structural feedback, and giga-voxel scalability, our framework advances beyond traditional image-based modeling, that are often limited in utility due to its reliance on unstructured information. Indeed, the data-driven model generation approach supports rapid modification and inherently provides design flexibility, thereby enabling broad structural exploration, accelerated prediction, and even inverse optimization.

Multiscale digital twin modeling was enabled through a logically structured, two-tiered process that mirrors both microstructural and mesoarchitectural features: 1) the generation of unit twins representing microstructures, and 2) the digital assembly of mesoarchitectures, both of which faithfully mirror physical reality. Especially, we highlight the high-speed, high-fidelity generation of microstructures through the closed-loop digital twin method, and the hierarchical organization of macroscopic geometric architectures by deriving logical and systematic assembly relationships from the 3D printing process. Previous work still fails to meet the high-fidelity mirroring of real microstructure because 3D models are generated from 2D geometry data or designed without cross-feedback with physical reality.[55–58]

As one of the key achievements of this study, we highlight the potential utility of our giga-voxel digital twin model in multiscale simulations. By successfully capturing both microscale fiber–matrix interfacial stresses and macroscale stress gradient

fields within a single multiscale model, our approach offers exceptional insight into the mechanics of composite systems, particularly those composed of anisotropic stiff fibers embedded within isotropic ductile matrices (Figure S38, Supporting Information). We demonstrate that the high-fidelity giga-voxel digital twin, when coupled with the rapid computational performance of FFT-based heterogenization, overcomes the longstanding trade-off between resolution and field-of-view. This enables the identification of microscale interfacial stresses within mesoscale geometric volumes (Table S4, Supporting Information). As a result, stress and strain fields within the fiber phase and the matrix phase were independently resolved within the giga-voxel framework. In contrast to conventional multiscale simulations that rely on sequential scale bridging across two or three hierarchical levels from microstructure to microarchitecture,[30] our model directly integrates structural details across multiple length scales within a unified computational domain.

We expect that FFT-based giga-voxel digital twins could provide a useful foundation for bridging micro- and macro-scale models in multiscale simulation (micro-macro stress bridging) (Figure S39, Supporting Information). In industrial and public research infrastructures, high-resolution tomography tools such as FIB-SEM, XRM, and TEM are now capable of generating giga-voxel-scale 3D datasets with exceptional geometric fidelity. The giga-voxel model serves as a bridge linking mesoscale microstructures to macroscopic material properties, enabling multiphysics and multiscale analyses that integrate mechanical, fluidic, electrical, and thermal phenomena within a unified simulation environment. By leveraging ultra-high-resolution voxel representations, it allows repeated non-destructive virtual experiments and facilitates digital investigations of regions that are experimentally inaccessible—such as nanoscale features or internal defects—thus providing a virtual experimental platform that complements or substitutes physical testing. In materials science, this approach plays a crucial role in characterizing the nano- and microstructures of fuel cells and batteries. In mechanical engineering, it supports structure–property correlation analyses and coupled thermo–mechanical–electrical simulations based on FEM and FFT frameworks. Furthermore, in architecture and cement science, giga-voxel digital twins can be applied to the structural analysis and degradation assessment of concrete and porous materials. Together, these use cases demonstrate the framework's broad applicability and its capacity to deliver quantifiable, practical benefits across multiple engineering domains.

However, the current analysis workflows remain largely manual or semi-automated, which fundamentally limits the processing speed, reproducibility, and reliability of large-scale data interpretation. We also recognize that broader applicability will depend on advances in software tools that can robustly support parameterization and geometry generation across diverse material systems. While several open-source alternatives exist for individual stages—such as tomographic reconstruction, segmentation, microstructural parameterization, geometric modeling, or numerical simulation—these solutions are typically dispersed across different platforms and require integration to reproduce a fully coherent workflow. To enable the practical use of giga-voxel data, a shift from fragmented and partially manual workflows toward fully automated, integrated analysis pipelines is essential. This requires coupling high-performance computing resources—particularly GPU-based parallelization—with data preprocessing, AI-driven segmentation, and simulation-based property prediction within a unified digital platform. While commercial tools partially support these tasks, the long-term solution lies in establishing scalable, cloud-integrated platforms that can handle end-to-end data flow, from 3D image reconstruction to multiscale performance evaluation. Such convergence of AI, simulation, and high-performance computing represents a key technological challenge, but also a critical pathway toward realizing truly data-driven digital twins for materials and devices. In the near future, we anticipate that such integrated digital platforms will enhance accessibility and foster a richer and more collaborative research ecosystem across materials and engineering communities.

4. Experimental Section

3D Printing of Composite Architectures: The characteristic process-induced microstructures of hierarchical composites were fabricated in a layer-by-layer scheme. First, the 3D printable feedstock material was prepared by mixing chopped basalt fiber (BF, Kamenny Vek, Moscow, Russia) and PLA resin (Polylactic acid, HANZENITH Co., China) with a cylindrical blender, followed by a melt extrusion process (Noztek Pro Extrusion System, Nozteck LTD, UK) using composite filaments with a diameter of 1.75 mm. BF was fed into the extruder equipment at a ratio of 10 vol% to PLA, the barrel temperature of the extruder was 220 °C, and the screw speed was 60 rpm during extrusion. The filament extruded from the nozzle was cooled by a cooling fan and wound onto a filament roll at a speed of 40 mm s^{-1} using a winder. CADian3D (Computer-Aided Design Package, IntelliKorea Co., Korea) was used to design the architecture of the sample. The anisotropic architectures of the text characters were designed according to the shape of "K," "A," "I," "S," and "T" fonts in a $9 \times 9 \times 1.5$ mm^3 space, consisting of 6 parallel lines of 0.5 mm diameter filaments filled in the width of the font. The castle architecture was designed in meso and macro scale with total dimensions of $40 \times 32 \times 12$ mm^3. The detailed configuration of the inner and outer geometric shapes was determined by considering the 0°, 45°, 90°, and 135° orientation directions of the 4 basic building blocks. When the design was completed, the CAD model in. stl format was sliced into thin layers using 3D Slicer software (Simplify3D, USA). In this process, the drawing path of the printing nozzle was manually adjusted. The layup architectures with helicoidal and quasi-isotropy stacking sequences were set up with the following orientation information. $[0°/45°/90°/135°/0°/45°/90°/135°]_{heli}$, $[0°/90°/45°/135°/135°/45°/90°/0°]_{QI}$.

The mesostructural architectures, including text characters and castle model, were set up to be filled in with contour printing from the outer to the core, following the geometric design. The specific infill patterns in the individual layers were determined using the pre-explored drawing paths during the slicing process as a reference. Each sample was sequentially printed with a single layer height of 0.5 mm by a commercial 3D printer (3DISON AEP, Rokit Co., Korea) equipped with nozzles of 0.4–0.6 mm in diameter. During printing, the nozzle temperature was heated to 220 °C and the platform temperature was maintained at 50 °C. The printing speed was set to a high speed of 50 mm s^{-1} for the high orientation of the embedded fibers. The mesostructural architectures with 100% packing density were prepared.

X-Ray Computed Microtomography (μCT): X-ray computed tomography (μCT) was used to explore in detail the internal microstructure of the 3D-printed BF/PLA composite structure. A high-resolution X-ray microscopy (Xradia 520 Versa, Zeiss, Germany) capable of providing a spatial resolution of 0.7 μm was used. The tomography workflow consists of image acquisition and image reconstruction steps. The sample stage was aligned between the X-ray source and detector, then extended to the region of interest by adjusting the source-sample distance and sample-detector

distance, respectively. Radiograph projection images were acquired while rotating the sample 360° at constant rotational intervals. The system was operated at an accelerating voltage of 50 keV and a power of 4 W, and each scan was performed with a low magnification objective lens of x0.4–x4 with pixel binning of 2. The exposure time of each projection was from 2.5 to 10 s, depending on the sample size. The collected projection images were reconstructed into 3D geometric tomography images with a voxel size of 1–4 µm using the Zeiss Scout-and-Scan control system. During image reconstruction, the motion drift of the sample and various image artifacts were corrected for accurate analysis.

Geometrical Characterization of Microstructure Using Geometry-Find AI: The geometrical parameters of the 3D-printed composite architecture were obtained through the computed tomography analysis, and the constituent materials were segmented, identified, and tracked using Geometry-Find AI, supported by GeoDict 2023 (Math2Market GmbH, Kaiserslautern, Germany). Geometry-Find AI, driven by a trained neural network, characterizes anisotropic geometries within tomographic microstructures of interest. Geometry-Find AI consists of AI Segmentation and Fiber-Find AI. The AI Segmentation learning method was U-net 2D and 3D model, and the number of Epochs (times), the depth of the U-net (levels), and the number of features (features) were treated as hyperparameters and set to 3, 2, and 16, respectively, as initially defined. The window size (subset size) was X = 52, Y = 52, and Z = 52. The brush tool was used to draw volume sections corresponding to fibers, matrix, and voids along the contrast boundary lines with a brush size of 5 to 15 pixels. This work was done in the same way for all XY, YZ, and ZX plane images. The training–segmentation cycle was repeated multiple times. For each training round, a total of 20 fiber, 10 matrix, and 20 void objects were manually annotated through brushing and labeling to construct the training dataset. The Intersection over Union (IoU) metric was used as a validation metric, comparing the predicted pixel occupancies of the segmented fibers, matrix, and voids with the manually measured pixel occupancies to determine the acceptance accuracy. As a result, fibers, matrix, and voids were successfully identified after five rounds of iterative data training. The identified geometric information was recorded in the data cloud, and material variability according to printing conditions was fed back. The geometrical parameters for the fibers and voids were quantitatively characterized based on the number of voxels occupied by corresponding objects using the submodules of FiberFind (AI) and PoroDict, respectively. The Fiber-Find AI used in this study is a pre-trained model provided by GeoDict. It was trained to predict fiber characteristics, such as volume fraction, length, and orientation, by taking pixel-level feature vectors extracted from segmented images as input. As a result, the fiber length, content, orientation, and distribution, as well as the void shape, content, and distribution within the unit cell structure, were accurately characterized at the microscale. Specifically, the function *Identify Fibers (AI)* was used to characterize the geometrical parameters for shape, length, and distribution of individual fibers. The functions Estimate fiber diameter/length identified the short diameter and long length of the fibers and then provided detailed information about the longitudinal length of the individual fibers. In detail, the fiber diameter is calculated by identifying the center of the sphere. The fiber length is defined as the longest chord length measured in all directions. Fiber diameter (d_f) and length (l_f) were obtained from the probability density function of the measured fibers within the region of interest, from which the length-to-diameter ratio (l_f/d_f) was derived. The function *Estimate fiber orientations* calculates fiber orientation in a subset block. The fiber orientation was computed by tracing the vector direction of the skeleton structure defined by both ends of the fiber. The longest chord length points to both ends of the fiber. For measurement, the volume was divided into spatial blocks (subsets), and orientation was computed within each block.

Digital Twin Voxel Modeling of Representative Micro-Scale Building Blocks: The digital twin process created a voxel-based virtual counterpart based on the tomographic reconstruction model of the 3D-printed composite architecture. The vast data cloud built by geometrical characterization of microstructures created digital representations of sub-volume structures with data-driven voxel modeling methods. FiberGeo, one of GeoDict's geometry modules, has the function of creating various types of fiber objects in a domain space. The domain space here is the digital voxel model generation space and corresponds to the 3D space of the unit volume of $0.5 \times 0.5 \times 0.5$ mm^3 in the microstructure of the tomographic reconstruction model. Since the microstructure of the 3D-printed composite shows a multi-scale architecture of the filament bundles containing embedded fibers inside, the matrix phase of the filament bundles was the first target volume for virtual representation. The digital unit twin proceeded in the following procedure. The region of interest on the matrix phase of the real sample was prepared as the domain space cropped to $0.5 \times 0.5 \times 0.5$ mm^3 of 4 µm-voxel resolution, and the matrix phase (yellow) was programmed to be considered as a working space for digitally generating fibers. Accordingly, the digital fibers (red) were created in matrix space (yellow), excluding void space (blue). (Note that the matrix space contains boundary lines (blue) of weak interfacial voids that identify the individual filaments.) The existing fibers in the matrix space were cleaned using the *voxel delete* function, and the matrix space in a pure state was prepared for new digital fibers—the shape and proportion of the interfacial voids that form the exterior shape of the object were kept in their original state without any editing work. The geometric parameters, such as fiber content, length, and orientation, recorded in the data cloud were used to create digital fibers in the domain space.

Users can then use the various optional functions provided by the FiberGeo module to set up fiber creation conditions and generate a virtual voxel model close to the real one. A library of pre-defined fiber modules with diverse geometries is stored in the system, allowing users to select an appropriate fiber shape tailored to the target architecture. Upon selection, users specify the geometric dimensions and spatial distribution characteristics of the fiber. The selected fiber morphology is then spatially assigned within the voxel domain according to the defined distribution parameters. By setting the random seed condition, an infinite number of digital representations of substructures were created in a non-overlapping way. Here, the basic building blocks of ⓐ' 0°, ⓑ' 45°, ⓒ' 90°, and ⓓ' 135° were digitally twinned according to the above workflow. Technically, the basic building block consists of an outer part representing the exterior shape of the object and an inner part representing the microstructure. The outer parts contain the contour filament with outer space, while the inner parts contain neighboring filaments with interfacial voids.

Digital Assembly of Giga-Voxel Meso-Scale Architectures: The giga-voxel mesostructural architectures were tailor-organized using millions of voxel micro-models as unit twin building blocks. The *Attach* function provided by the Process&LayerGeo module expands the model volume by attaching digital unit tons of the cubic volume to each of the six sides of ± X, ± Y, and ± Z. The building blocks in the extended volume have shared planes attached to each other in the *X*, *Y*, and *Z* directions. For example, a pair of building blocks of $0.5 \times 0.5 \times 0.5$ mm^3 can create one extended volume of $1.0 \times 0.5 \times 0.5$ mm^3 with the *X* plane attached. Specifically, the contacting surfaces were designed to have the same plane length, and the occupied region of the matrix (yellow) at the contacting surface remained almost consistent. Any dimensional errors at the contacting surfaces were negligible due to the giga-voxel volume's high resolution and could be ignored in most cases. If necessary, post-voxel edits are available to ensure consistency. These edits include functions to smooth the surface, remove objects, or redistribute objects as needed. The key factor in controlling consistency was maintaining a continuous orientation relationship on a hierarchical scale. To achieve this, the building blocks were connected parallel to their orientation, avoiding perpendicular connections. This ensured a seamless assembly and alignment of the microstructural components. In this way, the geometry processing tools first arrange the basic building blocks into 1D rows, expand them into 2D space, and stack them into a 3D architecture. The volume domains with the same structure or function are grouped into independent module units. These pre-grouped module units are named, saved, and reloaded when needed. In order to strategically organize the internal microstructure of the meso-architecture, we followed the sequential process in five steps: 1) Pre-search the drawing paths of the printer nozzle using the slicer program. 2) Strategically design the local microstructures by adjusting the drawing paths. 3) 3D print in the direction guided by the drawing paths. 4) The digital twin process identifies

the building block types and arrangements and precisely matches them with the drawing paths of the printing process. 5) The in-plane fiber orientations are determined along the drawing paths. The types and arrangements of the building blocks are linked to the drawing paths of the printing process through separate data processing: 1) Extracting the drawing path information from the G-code of the slicing model, 2) corresponding the orientation information to the building blocks, and 3) positioning the corresponding building blocks on the in-plane. Technically, the exterior shape of the object was described using the building blocks of the outer parts along the contour drawing path. The inner parts formed microstructures by connecting neighboring building blocks according to the infill pattern of the printing process.

Closed-Loop Feedback Mechanism: To quantitatively evaluate the statistical consistency between the physical and digital twins, this study introduces a weighted similarity index, denoted as S. This index integrates three statistical comparison terms—the mean discrepancy (f_μ), the standard deviation discrepancy (f_σ), and the distribution shape discrepancy based on the Kolmogorov–Smirnov (KS) distance (f_{KS})—to represent the degree of statistical divergence between two probability distributions in a single, normalized metric.

The weighted S-similarity index is defined as:

$$S = 1 - \frac{1}{3}\left(\omega_\mu f_\mu + \omega_\sigma f_\sigma + \omega_{KS} f_{KS}\right) \tag{1}$$

Where, f_μ, f_σ, and f_{KS} represent the normalized discrepancy metrics for the mean, standard deviation, and distribution shape, respectively. The weights. ω_μ, ω_σ, ω_{KS} (default: 1.0) can be adjusted to emphasize specific aspects depending on the objective. The weights are normalized such that:

$$\omega_\mu + \omega_\sigma + \omega_{KS} = 3 \tag{2}$$

For example, in cases where a higher sensitivity to distribution shape is desired, the value of ω_{KS}can be increased accordingly.

The mean discrepancy term is defined as:

$$f_\mu = \frac{|\mu_1 - \mu_2|}{x_{max} - x_{min}} \tag{3}$$

where μ_1 and μ_2 are the means of the physical and digital distributions, and $x_{max} - x_{min}$ is the normalization range (e.g., the range of fiber diameters).

The standard deviation term, reflecting distribution width differences, is computed as:

$$f_\sigma = \frac{|\sigma_1 - \sigma_2|}{|\sigma_1 - \sigma_2| + 1} \tag{4}$$

where, σ_1 and σ_2 are the standard deviations of the physical and digital distributions. This term ranges from 0 to 1, approaching 0 as the widths converge.

The distribution shape term, f_{KS}approximates the Kolmogorov–Smirnov (KS) distance between two normal distributions using:

$$D_{KS} \approx 2\Phi\left(-\frac{|\mu_1 - \mu_2|}{\sqrt{\sigma_1^2 + \sigma_2^2}}\right) \tag{5}$$

where, $\Phi(-)$ is the cumulative distribution function (CDF) of the standard normal distribution. The normalized form is:

$$f_{KS} = \frac{D_{KS}}{D_{KS} + 1} \tag{6}$$

Smaller values of f_{KS} value, indicate greater similarity in distribution shape. As the D_{KS} increases, the overall S value decreases.

If the computed S value falls below a predefined threshold (e.g., $S < 0.85$), the feedback mechanism is triggered. This may involve one of the following corrective actions: 1) modifying or removing erroneous model regions, 2) generating missing geometrical features, or 3) regenerating the entire model after parameter retuning.

Tomography Image-Based Simulation: The physical properties of the 3D-printed composite architecture were newly defined and added to the material library based on experimentally measured material property data of individual components. Based on the literature, BF was defined as an isotropic solid with a density of 2.67 g cm^{-3}. The mechanical properties of BF were obtained from tensile test results using a FAVIMAT+ textile testing machine (TexTechno, Monchengladbach, Germany) equipped with a 220 cN load cell. The basic physical properties, Young modulus, Shear modulus, and Poisson's ratio, were determined to be 87.5 GPa, 36.45 GPa, and 0.2 based on the strain–stress (S–S) curve data of the tensile sample, respectively. For the small/large deformation analysis, the plasticity model of exponential hardening was assumed, and the initial yield stress and first/second hardening parameters were calculated as 3.09, 13.99, and 1902.69 GPa, respectively. The PLA used as a matrix resin was defined as an isotropic solid material with a density of 1.25 g cm^{-3}, and its basic physical properties were defined as Young modulus of 3.4 GPa, shear modulus of elasticity of 1.27 GPa, and Poisson's ratio of 0.33. Initial yield stress and first/second hardening parameters were 0.006, 0.037, and 744.45 GPa, respectively. The mechanical properties of PLA were calculated by the S–S curve obtained from tensile testing on an Instron 5567A UTM instrument with a 30 kN load cell. Based on the above material library, the modulus and strength of composite materials were simulated by ElastoDict, a sub-module of GeoDict. A voxel-based Fast Fourier Transform (FFT) was used as the numerical solver model. The secondary-order fiber orientation tensor values obtained from the FiberFind module were used as input data to assume the orientation attributes of the reinforcing fibers in the composites. To reduce the computational cost for the giga-voxel model, a multiple-core parallelization process was used, and downsampling was utilized to decrease the computational elements. For maximum computational acceleration, 32 threads were involved in the parallel computation. Downsampling reduces the computational element by combining multiple voxels (4×4×4) into one voxel. To be able to use downsampling, the feature (e.g., fibers and grains) in each material must have a diameter of at least 4 voxels. The laminate theory was used to compute the composite voxels. When using laminate theory, the composite material properties are computed based on the laminate theory of the composite materials. With this option, direction-dependent properties are represented correctly. Therefore, each physical property of the constituent materials, such as fibers, voids, and matrix, contributes to the overall physical property determination. Based on the laminate theory, the displacement, strain, and stress of the composite voxel can be calculated as follows:

$$u(x, y, z) = u_0(x, y) + z\frac{\partial w}{\partial x} \tag{7}$$

$$v(x, y, z) = v_0(x, y) + z\frac{\partial w}{\partial y} \tag{8}$$

$$w(x, y, z) = w_0(x, y) \tag{9}$$

where, u, v, w define the displacement of the laminate. u_0, v_0, w_0 are the displacements of the neutral surface, and z is the thickness direction coordinate of the layer.

$$\varepsilon_{ij}(x, y, z) = \varepsilon_{ij}^0(x, y) + z\kappa_{ij}(x, y) \tag{10}$$

where, ε_{ij} defines the strain of the laminate. ε_{ij}^0 is the strain of the neutral surface, and κ_{ij} is the change in curvature of the layer.

$$\sigma_{ij} = Q_{ij} \cdot \varepsilon_{ij} \tag{11}$$

where, σ_{ij} defines the stress of the laminate. Q_{ij} is the orthotropic stiffness matrix, which reflects the direction and properties of the layer.

The modulus (stiffness) in the XY plane was calculated using the FeelMath Elasticity-VOX Solver. The load type was a strain for tensile (XX, YY, ZZ) and shear (XY, YZ, ZX) load cases, and the boundary condition was checked as a Periodic condition. For efficient calculation, strain increments of 0.01% were given. The uniaxial mechanical experiments were analyzed using a Deformation (LD) Solver. The load type was compression, the load direction was the *Z* axis, and the strain change was entered in 8 steps from 0% to 4% with a 0.5% increment. The boundary condition during compressive loading was checked as a Symmetry condition. For thermal expansion and shrinkage behavior, the macroscopic complex load experiment was performed. External environmental loads are applied to the RVE cubic volume. The RVE model is essentially an open structure, and the boundary conditions were set to symmetry to remove boundary interference. The mesoscale structures within the RVE volume consist of a solid phase, while the remaining volume is occupied by air. A temperature decrease step was entered from 50° to RT as a function of time increments with fixed strain and load conditions. The model resampling was chosen to maintain mass while volume changes. Other detailed conditions were the same as in the mechanical experiment.

In Situ X-Ray Microscopy Compression Test and Digital Image Correlation (DIC): The compression testing of the physical twin in the real world was performed using the micro test module within the X-ray microscopy system. The tomographic images were obtained while a load frame within the microtest module applied a specific compressive load on the sample. The sample was within a transparent glassy carbon tube of the micro test module, and a total of 1601 projection images were acquired over 180° with an exposure time of 2.5 s each. During scanning, the imaging system's accelerating voltage and power conditions were 50 keV and 3 W, respectively. The full-field displacement and strain fields were calculated using Digital Image Correlation (DIC, GOM Aramis system, Germany) for tomographic images obtained under the same load and similar experimental conditions as the simulation of the digital twin. During the image correlation analysis, the subset sizes of 96×96 and 64×64 pixels were determined by considering the characteristic length scale of the microstructure and the amount of deformation. A geometric mask was drawn along the contour line of the sample surface to exclude regions outside the measurement.

Supporting Information

Supporting Information is available from the Wiley Online Library or from the author.

Acknowledgements

This work was supported by the National Research Foundation of Korea (NRF) grant funded by the Korean government (MSIT) (RS-2023-00247245, RS-2022-NR068258). This work was also funded and conducted under the "Competency Development Program for Industry Specialists" of the Korean Ministry of Trade, Industry, and Energy (MOTIE) (P0017120). This work was also supported by the InnoCORE program of the Ministry of Science and ICT (N10250154).

Conflict of Interest

The authors declare no competing interests.

Data Availability Statement

The data that support the findings of this study are available from the corresponding author upon reasonable request.

Keywords

closed-loop digital twin, data-driven voxel modeling, giga-voxel, multi-scale, tomography

Received: June 4, 2025
Revised: October 14, 2025
Published online:

[1] A. Kantaros, D. Piromalis, G. Tsaramirsis, P. Papageorgas, H. Tamimi, *Appl. Syst. Innov.* **2022**, *5*, 7.
[2] A. S. Gladman, E. A. Matsumoto, R. G. Nuzzo, L. Mahadevan, J. A. Lewis, *Nat. Mater.* **2016**, *15*, 413.
[3] D. Nepal, S. Kang, K. M. Adstedt, K. Kanhaiya, M. R. Bockstaller, L. C Brinson, M. J. Buehler, P. V. Coveney, K. Dayal, J. A. El-Awady, L. C. Henderson, D. L. Kaplan, S. Keten, N. A. Kotov, G. C. Schatz, S. Vignolini, F. Vollrath, Y. Wang, B. I. Yakobson, V. V. Tsukruk, H. Heinz, *Nat. Mater.* **2023**, *22*, 18.
[4] G. B. Olson, *Science* **1997**, *277*, 1237.
[5] Z. Yang, C. Yu, M. J. Buehler, *Sci. Adv.* **2021**, *7*, abd7416.
[6] S. Bargmann, B. Klusemann, J. Markmann, J. E. Schnabel, K. Schneider, C. Soyarslan, J. Wilmers, *Prog. Mater. Sci.* **2018**, *96*, 322.
[7] M. Singh, E. Fuenmayor, E. P. Hinchy, Y. Qiao, N. Murray, D. Devine, *Appl. Syst. Innov.* **2021**, *4*, asi4020036.
[8] M. M. Rathore, S. A. Shan, D. Shukla, E. Bentafat, S. Bakiras, *IEEE Access* **2021**, *99*, 32030.
[9] G. Caldarelli, E. Arcaute, M. Barthelemy, M. Batty, C. Gershenson, D. Helbing, S. Mancuso, Y. Moreno, J. J. Ramasco, C. Rozenblat, A. Sánchez, J. L. Fernández-Villacañas, *Nat. Comput. Sci.* **2023**, *3*, 374.
[10] S. Shin, J. Eun, S. S. Lee, C. Lee, H. Hugonnet, D. K. Yoon, S.-H. Kim, J. Jeong, Y. Park, *Nat. Mater.* **2022**, *21*, 317.
[11] D. McLaughlin, M. Bierling, B. Mayerhöfer, G. Schmid, S. Thiele, *Adv. Funct. Mater.* **2023**, *33*, 2212462.
[12] H. Zhang, D. Ren, H. Ming, W. Zhang, G. Cao, J. Liu, L. Wang, J. Song, J. Qiu, J. Wang, X. He, H. Zhang, *Adv. Energy Mater.* **2023**, *13*, 2202660.
[13] M. A. Ali, Q. Guan, R. Umer, W. J. Cantwell, T. Zhang, *Compos. Sci. Technol.* **2022**, *217*, 109091.
[14] W. Huang, R. Xu, J. Yang, Q. Huang, H. Hu, *Compos. Struct.* **2021**, *256*, 113013.
[15] D. Oliver, B. Christian, *Front. Mater.* **2023**, *10*, 1154655.
[16] Y. Jakhotiya, M. R. Rahul, S. S. Chiddarwar, *Int. J. Interact. Des. Manuf.* **2024**, *18*, 7429.
[17] A. Marcato, J. E. Santos, C. Liu, G. Boccardo, D. Marchisio, A. A. Franco, *Energy Storage Mater.* **2023**, *63*, 102927.
[18] J. Song, R. C. Ihuaenyi, J. Lim, Z. Wang, W. Li, R. Fang, A. K. Ghamsari, H. Xu, Y. M. Lee, J. Zhu, *Energy Environ. Sci.* **2025**, *18*, 3129.
[19] S. Kim, H. Lee, J. Lim, J. Park, Y. M. Lee, *ACS Energy Lett.* **2024**, *9*, 5225.
[20] Y. Sun, Y. Ning, Z. Qiang, L. Xiang, Q. Liu, C. Zhang, G. Quan, Y. Zhang, B. Deng, G. Yin, T. Liu, J. Wang, S. Lou, *Angew. Chem., Int. Ed. Engl.* **2025**, *8*, abn5091.
[21] J. Song, S.-H. Lim, K.-G. Kim, N. Umirov, H. Lee, C. B. Dzakpasu, J. Lim, J. Nam, J. Park, J.-N. Lee, H. Munakata, K. Kanamura, S.-S. Kim, Y. M. Lee, *Adv. Energy Mater.* **2023**, *13*, 2204328.
[22] S. Jang, Y. Kang, H. Kim, J. Park, K. T. Lee, *Small Struct.* **2024**, *6*, 2400350.
[23] J. Park, K. T. Bae, D. Kim, W. Jeong, J. Nam, M. J. Lee, D. O. Shin, Y.-G. Lee, H. Lee, K. T. Lee, Y. M. Lee, *Nano Energy* **2021**, *79*, 105456.
[24] J. Park, K. T. Kim, D. Y. Oh, D. Jin, D. Kim, Y. S. Jung, Y. M. Lee, *Adv. Energy Mater.* **2020**, *10*, 2001563.

[25] K. Maksymenko, A. K. Clarke, I. M Guerra, S. Deslauriers-Gauthier, D. Farina, *Nat. Commun.* **2023**, *14*, 1600.
[26] W. Huang, P. Causse, H. Hu, F. Trochu, *Polym. Compos.* **2020**, *41*, 1341.
[27] S. Fajal, W. Mandal, A. Torris, D. Majumder, S. Let, A. Sen, F. Kanheerampockil, M. M. Shirolkar, S. K. Ghosh, *Nat. Commun.* **2024**, *15*, 1278.
[28] S. Yu, J. Y. Hwang, S. H. Hong, *Compos. B.* **2020**, *187*, 107839.
[29] H. Zhao, Z. Yang, L. Guo, *NPG Asia Mater* **2018**, *10*, 1.
[30] J. Fish, G. J. Wagner, S. Keten, *Nat. Mater.* **2021**, *20*, 774.
[31] A. Doitrand, C. Fagiano, F.-X. Irisarri, M. Hirsekorn, *Compos. A* **2015**, *73*, 143.
[32] G. Fang, B. E. Said, D. Ivanov, S. R. Hallett, *Compos. A* **2016**, *80*, 270.
[33] W. Jiang, W. Liao, T. Liu, X. Shi, C. Wang, J. Qi, Y. Chen, Z. Wang, C. Zhang, *Mater. Des.* **2021**, *204*, 109655.
[34] N. Aage, E. Andreassen, B. Lazarov, O. Sigmund, *Nature* **2017**, *550*, 84.
[35] F. Schnös, D. Hartmann, B. Obst, G. Glashagen, *Int. J. Adv. Manuf. Technol.* **2021**, *115*, 275.
[36] L. F. Bez, R. Leiderman, A. Souza, R. B. de V. Azeredo, A. M. B. Pereira, *Transp. Porous. Med.* **2024**, *151*, 2405.
[37] F. Soldevila, A. J. M. Lenz, A. Ghezzi, A. Farina, C. D'Andrea, E. Tajahuerce, *Opt. Lett.* **2021**, *46*, 4312.
[38] S. Wu, L. Guo, Z. Li, T. Zheng, J. Ding, F. Jia, *Compos. Sci. Technol.* **2025**, *261*, 111021.
[39] W. Hu, H. Cheng, S. Wang, H. Cheng, Y. Cheng, K. Zhang, B. Liang, *Compos. Struct.* **2024**, *342*, 118246.
[40] F. Sosa-Rey, C. Vella, A. Lingua, J. Pierre, N. Piccirelli, D. Therriault, M. Lévesque, *Compos. Sci. Technol.* **2023**, *243*, 110261.
[41] J. L. Mari, *Int. Conf. Discr. Geom. Comput. Imag.* **2009**, *5810*, 326.
[42] D. Qi, N. Milef, S. De, *Vis. Comput.* **2021**, *37*, 1113.
[43] S. Yu, Y. H. Hwang, K. T Lee, S. O. Kim, J. Y. Hwang, S. H. Hong, *Adv. Sci.* **2021**, *25*, 2103561.
[44] S. Yu, H. Bale, S. Park, J. Y. Hwang, S. H. Hong, *Compos. B.* **2021**, *224*, 109184.
[45] L. A. Shaw, F. Sun, C. M. Portela, R. I. Barranco, J. R. Greer, J. B. Hopkins, *Nat. Common.* **2019**, *10*, 291.
[46] X. Xie, S. Maharjan, S. Liu, Y. S. Zhang, C. Livermore, *Micromachines.* **2020**, *11*, 2.
[47] S. Babaee, J. Shim, J. C. Weaver, E. R. Chen, N. Patel, K. Bertoldi, *Adv. Mater.* **2013**, *25*, 5044.
[48] A. Farzaneh, N. Pawar, C. M. Portela, J. B. Hopkins, *Nat. Commun.* **2022**, *13*, 1041.
[49] J. N. Grima-Cornish, J. N. Grima, D. Attard, *Int. J. Mech. Mater. Eng.* **2021**, *16*, 4.
[50] B. G. Compton, J. A. Lewis, *Adv. Mater.* **2014**, *26*, 5930.
[51] J. H. Panchal, S. R. Kalidindi, D. L. McDowell, *Comput. Aided Des.* **2013**, *45*, 4.
[52] F. Francqueville, P. Gilormini, J. Diani, *Int. J. Solids Struct.* **2019**, *158*, 277.
[53] H. Zhou, D. Z. Zhang, N. He, M. Zhao, *Compos. Struct.* **2023**, *321*, 117294.
[54] Y. Jia, K. Liu, X. S. Zhang, *Nat. Commun.* **2024**, *15*, 4072.
[55] X. Shang, Z. Liu, J. Zhang, T. Lyu, Y. Zou, *Mater. Today* **2023**, *70*, 71.
[56] S. Kench, I. Squires, A. Dahari, F. B. Planella, S. A. Roberts, S. J. Cooper, *Matter* **2024**, *7*, 4260.
[57] J. Zhong, J. An, D. Wu, N. Gao, L. Liu, Z. Wang, F. Meng, X. Zhou, T. Fan, *Int. J. Mech. Sci.* **2024**, *281*, 109550.
[58] K. Lertkiatpeeti, C. Janya-Anurak, V. Uthaisangsuk, *Comput. Mater. Sci.* **2024**, *245*, 113311.